Enhanced metal-support interaction boosted industrial electrocatalytic water splitting performance of supported Ru nanoparticles on Ni3N/NiO heterojunction

Rui Liu
Beijing Institute of Technology
Mingzi Sun
Hong Kong Polytechnic University https://orcid.org/0000-0001-5136-7265
Xiangjian Liu
Beijing Institute of Technology
Zunhang Lv
Beijing Institute of Technology
Xinyu Yu
Beijing Institute of Technology
Jinming Wang
Beijing Institute of Technology
Yarong Liu
Beijing Institute of Technology
Liuhua Li
Beijing Institute of Technology
Wenxiu Yang
Bolong Huang
Hong Kong Polytechnic University https://orcid.org/0000-0002-2526-2002
Xiao Feng
Beijing Institute of Technology https://orcid.org/0000-0002-3212-3051
Bo Wang (bowang@bit.edu.cn)
Beijing Institute of Technology https://orcid.org/0000-0001-9092-3252

Article

Keywords:

Posted Date: August 26th, 2022

DOI: https://doi.org/10.21203/rs.3.rs-1986860/v1

Abstract

Developing highly efficient and stable hydrogen production electrocatalysts for water splitting at industrial current densities remains a great challenge. Herein, we fabricated Ru nanoparticle-anchored ultrathin Ni3N/NiO heterostructure nanosheets (Ru-Ni3N/NiO) for efficient electrochemical water splitting (EWS). Density function theory (DFT) calculations demonstrated that the formation of Ni3N/NiO-heterostructures improve the structural stability, electronic distributions, and orbital coupling of Ru-Ni3N/NiO compared to single-phase-metal-carrier catalysts (Ru-Ni3N and Ru-NiO), which increases the electroactivity and further lead to strongly decreased energy barriers for EWS. As a proof-of-concept, the catalyst with oriented 2D nanosheet array morphology, mono-dispersed Ru nanoparticles, and strong metal-support interaction (MSI) was successfully constructed. Furthermore thus-obtained Ru-Ni3N/NiO-based EWS devices can realize an industrial current density of 1000 mA cm−2 at 1.74 V and 1.80 V under alkaline pure water and seawater conditions, respectively. Additionally, high durability of 1000 h (@ 500 mA cm−2) can also be achieved in the alkaline pure water EWS device.

Introduction

Hydrogen is an ideal clean and renewable energy carrier, leading to its potential utilization in the future **energy storage/conversion** system[1-3]. Yet the most common industrial hydrogen-producing methods, such as natural gas and methanol reforming, will produce large amounts of carbon dioxide, which is difficult to meet the requirement of low-carbon-target[4]. Electrocatalytic water splitting (EWS) is a promising way to produce high purity hydrogen, but the efficiency of the EWS is kinetically controlled by the cathodic hydrogen evolution reaction (HER) and anodic oxygen evolution reaction (OER)[5-8]. Up to now, commercial Pt/C and IrO_2 materials have been regarded as efficient catalysts for HER and OER, but their scarcity, poor-stability and high cost hinder their practical application in the EWS[9-11]. Currently, transition metal (Ru, Ni, Co, Cu)-based composites have shown high conversion efficiencies for EWS, yet most of them are mono-functional nano-catalysts[11-17], which not only increases the cost and complexity of the EWS process, but also affects the catalytic performance due to the crossover effect. More importantly, these catalysts still own limited EWS performance at large current densities (≥ 500 mA cm^{-2})[18, 19]. Hence, design and development of low-cost and high-performance bi-functional catalysts are urgently required for EWS.

Supported metal nanocatalysts, with uniform dispersed metal nanoparticles, controlled metal-support interaction (MSI) and comparable catalytic performance, have attracted extensive attention in the field of EWS[20, 21]. Specially, Ru-based supported nanomaterials show increasing potential due to their low-price and Pt-like EWS performance. Yet most of the reported supports such as metal oxides[13, 22, 23], phosphide [15, 24-26], hydroxide[27-29] and heteroatoms doped carbon materials[30, 31], are homogeneous carriers with less exposed active sites and unsatisfied MSI, which ultimately hinders the achievement of efficient theoretical catalytic performance. Consequently, designing a novel metal-based heterojunction

carrier with tuned MSI can be essential to develop a high-performance supported Ru catalyst for EWS at industrial current densities. However, this is rarely explored and extremely challenging.

Herein, we proposed a facile heterojunction carrier induced strategy to optimize the MSI and the EWS activity at industrial current densities. Density functional theory (DFT) calculations reveal that the electrocatalytic reaction is promoted when Ru nanoparticles are loaded on Ni_3N/Ni heterojunction carriers than on single metal-based carriers such as Ni_3N and NiO. The formation of heterostructure among Ru nanoparticles, Ni_3N, and NiO has led to evident electronic modulations. The unique interactions within the heterostructure enable the bifunctional electrocatalysis through the d-band center optimizations of both Ru and Ni sites, which is able to guarantee efficient HER and OER performances. To realize this, the target catalysts were assembled by metallic Ru nanoparticles and ultrathin Ni_3N/NiO heterojunction nanosheet arrays through a spontaneous redox reaction at room temperature (denoted as Ru-Ni_3N/NiO). Benefiting from the morphological and structural advantages of rich exposed active sites, efficient mass transfer, and enhanced MSI, the Ru-Ni_3N/NiO catalyst exhibited outstanding electrochemical HER and OER activity with an overpotential of only 190 mV and 385 mV at 1000 mA cm^{-2}, respectively. Meanwhile, it requires extremely low voltage of 1.74 V and 1.80 V to achieve a current density of 1000 mA cm^{-2} in overall alkaline water and seawater splitting devices, respectively. And the alkaline water splitting device could maintain good stability at 500 mA cm^{-2} for 1000 h.

Results

Electronic Structure Investigations. A novel model with Ru-Ni_3N/NiO three-phase heterogeneous interface was firstly constructed together with the Ru-Ni_3N, Ru-NiO, and Ni_3N/NiO models (Supplementary Fig. 1). The bonding and anti-bonding orbitals distributions near the Fermi levels (E_F) have shown different behaviors for the heterostructure systems (Fig. 1a-c). Within Ru-Ni_3N, it is noted that the anti-bonding orbitals are dominated by the anchoring Ru NPs while the bonding orbitals mainly locate in Ni sites with limited contributions from Ru NPs. For Ru-NiO, we notice the structural instability has evidently increased due to the

evident distortion in NiO. Although the bonding orbitals become more electron-rich in Ru NPs, the lower lattice stability may hinder the electrocatalysis performances. In comparison, the Ru-Ni_3N/NiO heterostructure displays a highly electron-rich feature on the surface and Ru NPs to guarantee efficient electron transfer with a stable structure. The strong orbital coupling between bonding and anti-bonding orbitals results in superior electroactivity for both oxidation and reduction reactions. The detailed electronic structures are demonstrated by the partial density of states (PDOS) for these three heterostructures Ru-Ni_3N, Ru-NiO, and Ru-Ni_3N/NiO systems (Fig. 1d-f). Notably, all Ni-3d orbitals show evident a sharp peak near the E_F, which play as the dominant sites for proton binding during the HER. Meanwhile, Ru-4d orbitals all exhibit a broad peak with e_g-t_{2g} splitting, which plays as the main active site for water-dissociation under the alkaline environment. Notably, N-2p and O-2p orbitals are both located at

the deeper position, which act as the electron reservoir during electrocatalysis. For Ru-Ni_3N/NiO, it is noted that orbital coupling between O and N further strengthens the site-to-site electron transfer within the heterostructure. The site-dependent PDOSs further reveal the electronic modulation induced by the heterostructure (Fig. 1g). For Ru NPs, we notice that from the interface with Ni_3N/NiO to the NP surface, the e_g-t_{2g} splitting is strongly alleviated from 4.70 eV to 1.24 eV, indicating much alleviated barriers for electron transfer, which is able to accelerate the water dissociation process. Meanwhile, the Ni-3d orbitals display different behaviors in Ni_3N and NiO components (Fig. 1h). Within the Ni_3N, the formation of the interface with NiO has led to the upshifting of the Ni-3d orbitals with improved electroactivity. The introduction of Ru NPs on the surface further upshifts the Ni-3d orbitals to guarantee efficient electron transfer. In comparison, the Ni-3d orbitals in NiO experience a volcano trend (Fig. 1i). From the bulk to the surface, Ni-3d orbitals exhibit a gradual upshifting trend. For the Ni sites at the interface with Ni_3N and Ru NPs, their 3d orbitals show slight downshifting. Such a volcano trend indicates that the formation of heterostructures enables subtle modulations of the electroactivity. The d-band center of Ru in Ru-Ni_3N/NiO balances the electroactivity of water dissociation and binding of OH* (Fig. 1j). In contrast, the d-band center of Ni sites shows a gradual downshifting trend from Ru-Ni_3N to Ru-Ni_3N/NiO, which optimizes the overbinding effect of protons. Thus, it can be inferred that Ru-Ni_3N/NiO may have very excellent electrocatalytic EWS activity.

Synthesis and morphological characterizations. To further validate experimentally the superior activity of Ru NPs on Ni_3N/NiO substrates with heterogeneous structures, we designed and prepared the obtained Ru- Ni_3N/NiO catalysts. The synthetic route of Ru-Ni_3N/NiO electrocatalysts was exhibited in Fig. 2a (see experimental details in the Methods). First, the ultrathin $Ni(OH)_2$ nanosheet arrays were in-situ grown on the

3D porous Ni foam (NF) through simple acid corrosion engineering. After annealing in NH_3, the $Ni(OH)_2$ nanosheets were transformed into Ni_3N/NiO heterostructured nanosheets. Subsequently, Ru nanoparticles were formed onto the heterostructured Ni_3N/NiO nanosheets by a spontaneous redox reaction ($2Ru^{3+} + 3Ni \rightarrow 2Ru + 3Ni^{2+}$) in $RuCl_3$ solution at room temperature[12, 32].

The scanning electron microscopy (SEM) characterization indicates the successful formation of the uniform $Ni(OH)_2$ ultrathin nanosheet arrays on the NF surface with a height of about 1 ~ 2 μm (Fig. 2b and Supplementary Fig. 2) and a thickness of ~ 1.5 nm (Fig. 2c). After low temperature annealing in NH_3 atmosphere, the obtained Ni_3N/NiO material maintains the nanosheet arrays morphology yet with a rougher and defect-rich surface (Supplementary Figs. 3 and 4). As can be observed in Supplementary Fig. 5, the successful synthesis of Ni_3N/NiO heterostructured nanosheets was confirmed by the high-resolution transmission electron microscopy (HRTEM) characterization. And monodisperse Ru nanoparticles can be found on the surface of the ultrathin Ni_3N/NiO nanosheet (Fig. 2d, e and Supplementary Fig. 6). Meanwhile, the morphology of the Ru-Ni_3N/NiO composite is strictly affected by the immersion time, where too long or too short impregnation time is not conducive to the formation of

Ru-Ni_3N/NiO (Supplementary Fig. 7). The HRTEM image of Ru-Ni_3N/NiO (Fig. 2f and Supplementary Fig. 8) shows that a three-phase heterogeneous interface (dotted line) formed in the resulting Ru-Ni_3N/NiO catalyst and the lattice fringes are mainly ascribed to the (101) plane of Ru, the (002) plane of Ni_3N, and the (111), (200) planes of NiO. The energy-dispersive spectra (EDS) analysis results further indicate that the nanoparticles loaded on the Ni_3N/NiO nanosheets are Ru (Fig. 2g). The high-angle annular dark-field scanning transmission electron microscopy (HAADF-STEM) and the corresponding EDS elemental mapping images demonstrate the successful introducing of Ni, O, N and Ru elements in Ru-Ni_3N/NiO (Fig. 2h).

Structure characterization. The composition and surface valence of the obtained catalysts were investigated by X-ray diffraction (XRD) and X-ray photoelectron spectroscopy (XPS). The XRD peaks of Ru-Ni_3N/NiO in Fig. 3a are corresponded well with Ru (JCPDS 06-0663), Ni_3N (JCPDS 10–0280), and NiO (JCPDS 44-1159), confirming the formation of these three phases in Ru-Ni_3N/NiO. The XPS survey spectra verified the elemental composition and content of Ru-Ni_3N/NiO and Ni_3N/NiO (Fig. 3b and Supplementary Table 1). As

indicated in the high-resolution Ru 3p spectrum of Ru-Ni_3N/NiO (Fig. 3c), two peaks with binding energies (BEs) of 463.38 eV and 484.38 eV are corresponded to Ru $3p_{3/2}$ and Ru $3p_{1/2}$ of metallic Ru, respectively, demonstrating the existence of metallic Ru (0)[33, 34]. As shown in Fig. 3d, the high-resolution Ni 2p spectra of Ru-Ni_3N/NiO and Ni_3N/NiO display the typical peaks of Ni $2p_{3/2}$ (856.08 eV) and Ni $2p_{1/2}$ (873.48 eV)[12]. In comparison of Ni_3N/NiO, Ni peaks of Ru-Ni_3N/NiO shifted to a higher energy level by 0.2 eV, demonstrating the strong electronic MSI between metallic Ru and Ni_3N/NiO carrier. And this MSI result can be further verified by the positive shifts of 0.2 eV in high-resolution N 1s spectra of Ni_3N/NiO and Ru-Ni_3N/NiO (Fig. 3e). The high-resolution O 1s spectrum of Ni_3N/NiO was assigned to three peaks, which are metal-oxygen bonds (O_{Ni-O}), low coordination oxygen ions (O_{OL}), and water adsorbed on the material surface (O_{H-OH})[35, 36]. Among them, the O_{OL} peak centered at 531.5 eV can be attributed to the presence of defective sites. And the O_{OL} peak ratio would greatly increase to 90.5% in the Ru-Ni_3N/NiO sample, indicating the formation of much more defect sites in Ru-Ni_3N/NiO(Fig. 3f)[37].

Electrochemical HER. The HER properties of different samples were investigated in N_2-saturated 1.0 M KOH solution, and electrochemical tests were performed in a three-electrode system. The *iR*-compensated linear scanning voltammogram (LSV) curves for HER over Ru-Ni_3N/NiO, Ru-Ni_3N, Ru-NiO, Ni_3N/NiO, commercial Pt/C and NF can be observed in Fig. 4a. Among them, the target Ru-Ni_3N/NiO catalyst exhibits the best HER performance with overpotentials of 15 mV, 46 mV, and 63 mV at current densities of 20 mA cm^{-2}, 50 mA cm^{-2} and 100 mA cm^{-2}, respectively. And compared to most of the reported HER catalysts, Ru-Ni_3N/NiO exhibit excellent activity at low potential (Supplementary Table 2). More importantly, Ru-Ni_3N/NiO also shows surprising performance at industrial current densities, with overpotentials of only 121 mV and 190 mV at current densities of 500 mA cm^{-2} and 1000 mA cm^{-2},

demonstrating its potential for industrial applications. Furthermore, the overpotential *vs.* Tafel slope (Fig. 4b and Supplementary Fig. 10) reveal Ru-Ni_3N/NiO performs Pt-like HER kinetics with a Tafel slope of 45.1 mV dec^{-1}, which is much better than other contrast samples. (Ru-Ni_3N (47.8 mV dec^{-1}), Ru-NiO (59.9 mV dec^{-1}), Ni_3N/NiO (98.8 mV dec^{-1}), commercial Pt/C (51.85 mV dec^{-1}) and NF (118 mV dec^{-1}) (Fig. 4b and Supplementary Table 3).

Double-layer capacitance (C_{dl}) was usually applied to evaluate the electrochemical specific area (ECSA) of different modified electrodes (Supplementary Fig. 11). The Ru-Ni_3N/NiO electrode owns largest C_{dl} of 311.7 mF cm^{-2} among all contrast samples (Supplementary Fig. 12), indicating more electrochemical active

sites can be exposed in Ru-Ni_3N/NiO. Meanwhile, the lowest charge transfer resistance (R_{ct}) of Ru-Ni_3N/NiO was gained by the electrochemical impedance spectroscopy (EIS) tests, revealing a desirable electron transport ability in Ru-Ni_3N/NiO (Supplementary Fig. 13 and Supplementary Table 4). Furthermore, extremely small contact angle of Ru-Ni_3N/NiO (~ 0°) can greatly promote rapid penetration and mass transfer of the electrolyte in the Ru-Ni_3N/NiO electrode (Supplementary Fig. 14).

Subsequently, the electrochemical long-time stability of Ru-Ni_3N/NiO was investigated by chronopotentiometry (CP) as well as accelerated degradation test (ADT). And the polarization curve of Ru-Ni_3N/NiO hardly shifts after 15,000 CV cycles (Fig. 4c). As for the CP test, Ru-Ni_3N/NiO can operate better stability than the Pt/C catalyst at different current density (100 mA cm^{-2} and 500 mA cm^{-2}) (Supplementary Figs. 15–17). After the durability test, the morphology and valence state of Ru-Ni_3N/NiO with no change could be observed by SEM and XPS (Supplementary Figs. 18–19), further demonstrating its superior robustness. These results indicated that large ECSA and rapid charge/mass transfer capability of Ru-Ni_3N/NiO synergistically prompt it enhanced HER catalytic activity and stability.

Electrochemical OER. Meanwhile, the Ru-Ni_3N/NiO catalyst exhibits better OER performance with a smaller over potential at 100 mA cm^{-2} current density (η_{100} = 261 mV), than Ru-Ni_3N (η_{100} = 321 mV), Ru-NiO (η_{100} = 337 mV), Ni_3N/NiO (η_{100} = 379 mV), RuO_2 (η_{100} = 404 mV), and NF (η_{100} = 451 mV) samples (Fig. 4d). And a high current density up to 1000 mA cm^{-2} can be achieved at an overpotential of 385 mV for Ru-Ni_3N/NiO due to the unique structural advantage and the enhanced MSI. More significantly, Ru-Ni_3N/NiO has the lowest tafel slope compared to all the comparison samples synthesized (Fig. 4e and Supplementary Fig. 10, Supplementary Table 3), which can be comparable to the reported state-of-art OER catalysts (Supplementary Table 5). The Ru-Ni_3N/NiO catalyst also shows excellent catalytic stability for OER with no significant change after 15000 CV cycles and CP stability test (> 100 h) (Fig. 4f and Supplementary Figs. 20–21). After the OER long-term durability test, the original nanosheet array structure was maintained, and slight of the Ru nanoparticles were oxidized to Ru^{4+}, thus promoting the OER activity (Supplementary Figs. 22–23).

Reaction Trends by DFT Calculations. DFT calculations were used to further reveal the intrinsic relationship between the modulated electronic structure and the superior performances of Ru-Ni_3N/NiO under alkaline conditions. First, the reaction energy of HER has been compared (Fig. 4g). Notably, the initial adsorption of water and protons are both energetically favored for all three heterostructure systems. The dissociation of water is the rate-determining step (RDS) of the HER, where the energy barrier is 0.83, 0.73, and 0.60 eV for Ru-Ni_3N, Ru-NiO, and Ru-Ni_3N/NiO, respectively. Meanwhile, the reaction energy change of Ru-Ni_3N and Ru-NiO are similar, which are smaller than that of the Ru-Ni_3N/NiO, supporting the superior performances of Ru-Ni_3N/NiO for the HER. Then, the reaction energy of OER is also compared, where the RDS is the conversion from O* to OOH* with the largest energy barrier (Fig. 4h). Ru-Ni_3N/NiO displays the smallest barrier of 1.43 eV for the RDS, leading to the highest OER performance. With the applied equilibrium potential (U = 1.23 V), the overpotential has been estimated to be 0.20 V for Ru-Ni_3N/NiO, which is much alleviated than that of Ru-Ni_3N, Ru-NiO, supporting the improved OER performances (Fig. 4i). The introduction of Ru nanoparticles on Ni_3N/NiO heterojunction carriers and the formation of a unique heterostructure resulted in superior electrocatalysis as the electronic structures were optimized and the energy barrier of RDS for HER and OER has been significantly alleviated.

Performance in water electrolyzers device. Encouraged by the excellent catalytic activity of Ru-Ni_3N/NiO for both HER and OER, a two-electrode system was assembled using the Ru-Ni_3N/NiO as both cathode and anode (Ru-Ni_3N/NiO(+,-)) for overall water splitting. As shown in Fig. 5a, only a small cell voltage of 1.74 V is needed to achieve an industrial current density (1000 mA cm^{-2}) in this Ru-Ni_3N/NiO(+,-)-based overall water splitting device. Meanwhile, the Ru-Ni_3N/NiO(+,-) electrolyzer powered by a 1.5 V battery can work well in 1.0 M KOH with significant bubble release (Fig. 5b). Moreover, the Ru-Ni_3N/NiO(+,-) electrolyzer showed surprising durability, maintaining a cell voltage of 1.74 V for over 1000 h at industrial current density of 500 mA cm^{-2} with almost no significant degradation, further confirming the excellent stability of the catalyst (Fig. 5c).

To explore their practical application potential, the Ru-Ni_3N/NiO catalyst were tested in the alkaline seawater (0.5 M KOH + seawater), which display comparable HER and OER activity compare to the results in 1.0 M KOH solution (Supplementary Figs. 24–25). More importantly, Ru-Ni_3N/NiO(+,-) electrolyzer in alkaline SW and alkaline urea (1.0 M KOH + 0.33 M urea) could also achieve a good electrochemical performance (with a potential of only 1.75 V and 1.53 V at 500 mA cm^{-2}) and long-time durability (@ 500 mA cm^{-2}, 50 h), respectively (Supplementary Figs. 26–27). All these results prove that the obtained Ru-Ni_3N/NiO catalyst is one of the best reported bifunctional catalysts for the EWS process (Fig. 5d and Supplementary Table 6), and in particular it exhibits excellent performance at a high current densiy (500 mA cm^{-2}) (Supplementary Table 7).

Conclusion

In summary, based on DFT calculations, the formation of Ni_3N/NiO heterostructure in Ru-Ni_3N/NiO can result in a highly electroactive surface with modulated d-band centers of both Ru and Ni sites, which not only ensures the high electroactivity but also alleviates the overbinding effect. With the optimized electronic structures, the energy barrier of RDS for HER and OER has been significantly alleviated to achieve outstanding EWS performance in alkaline media. The heterogeneous carrier effect and the MSI between Ru nanoparticles and heterojunction Ni_3N/NiO lead to rich exposed surface-active sites, efficient mass transfer, excellent hydrophilicity, and structural stability of Ru-Ni_3N/NiO. The optimal Ru-Ni_3N/NiO(+,-) electrolyzer also exhibited excellent electrocatalytic EWS performances in alkaline pure water (1.74 V) and even alkaline seawater (1.80 V) at an industrial current density of 1000 mA cm^{-2}. This report provides fundamental and technological insights for developing highly efficient Pt-free self-supported catalysts for renewable energy storage/conversion devices.

Methods

Preparation of Ru-Ni_3N/NiO, Ru-NiO, and Ru-Ni_3N. First, a piece of NF (4 × 1 cm^2) was immersed into 3 M HCl with ultrasonic treatment 15 min. Then, it was transferred to a sealed glass bottle with 0.2 mM HCl aqueous solution (20 mL) and heated to 80 °C under stirring for 20 h. After that, $Ni(OH)_2$ precursor was obtained through washing with ultrapure water, and dry in oven at 50 °C. The $Ni(OH)_2$ electrode was placed in a quartz boat and calcinated at 350 °C for 3 h in NH_3 atmosphere, Ni_3N/NiO was obtained. Additionally, the $Ni(OH)_2$ electrodes were calcinated in air at 350°C for 3h and in NH_3 at 450°C for 3h to obtain NiO and Ni_3N electrodes respectively. Then, all the obtained materials after calcination were immersed in 10 mg mL^{-1} RuCl3 solution for 1 h. Each sample was subsequently removed from the solution, washed with ultrapure water for three times, and dried in air to obtain Ru-Ni_3N/NiO, Ru-NiO, Ru-Ni_3N.

Material characterization. The crystallographic information of the prepared products was analyzed by powder XRD on a Rigaku MiniFlex600 Powder X-ray Diffractometer with a Cu Kα X-ray radiation source (λ = 0.154056 nm). X-ray photoelectron spectroscopy (XPS, PHI QUANTERA-II SXM) with an Al Kα X-ray radiation source (0.68 eV) was used to investigate the element composition and valence information of the sample surface. SEM images were captured in JEOL model S-4800 scanning electron microscope operated at 5 kV voltage. TEM measurements were conducted on a JEM-2010 microscope operated at 200 kV and equipped with an EDS mapping were acquired from Bruker Quantax. HRTEM and elemental mapping were performed on a Hitachi HD2700C (200 kV) microscope.

Electrochemical measurements. All electrochemical measurements were performed in a three-electrode cell with the connection of an electrochemical workstation CHI660E. The Ru-Ni_3N/NiO were cut into 0.5 × 0.5 cm^2 as the working electrode, graphite rod as the counter electrode, and Ag/AgCl (with saturated KCl aqueous solution) as the reference electrode. HER and OER were tested in N_2-saturated and O_2-saturated 1.0 M KOH solutions, respectively. All the potentials were recorded relative to the reversible hydrogen

electrode (*vs*. RHE) according to the Nernst equation: $E_{RHE} = E_{Ag/AgCl} + 1.021$ V (Supplementary Fig. 9). The polarization curves of HER and OER were measured by LSV with 95% *iR*-compensation at the sweep rate of 5 mV s^{-1}. Overall water splitting performances was carried out in a standard two-electrode system using bifunctional Ru-Ni_3N/NiO as both anode and cathode with 90% *iR*-compensation. The frequency setting range of the EIS test is from 100 kHz to 0.01 Hz. C_{dl} was estimated from the CV method at various scan rates (v = 60, 70, 80, 90, 100 mV s^{-1}) in the non-Faraday zone, and C_{dl} was given in the following equation: $\Delta j = j_{anodic} - j_{cathodic} = 2 \times v \times C_{dl}$. The ECSA of the obtained catalysts were calculate by the following calculation formula: ECSA = C_{dl} / C_s (C_s = 60 μF/cm^2). Long-term stability of catalyst was both investigated by ADT and CP. ADT was conducted by applying CV from 0 V ~ -0.4 V (HER) and 1.2 V ~ 1.7 V (OER) at a scan rate of 100 mV s^{-1} with 15,000 cycles. Besides, all of the CP tests were held at a current density of 100, 500, and 1000 mA cm^{-2} for long-term stability tests without *iR*-compensation.

Calculation Setup. To investigate the electrocatalysis performances of different heterostructures, DFT calculations have been introduced and performed by the CASTEP packages[38]. For the functionals, the generalized gradient approximation (GGA) and Perdew-Burke-Ernzerhof (PBE) functionals are selected for the accurate descriptions of exchange-correlation interactions[39-41]. For the geometry optimizations, we have selected the ultrasoft pseudopotentials and set the plane-wave basis cutoff energy to 380 eV for all the heterostructures. Meanwhile, the Broyden-Fletcher-Goldfarb-Shannon (BFGS) algorithm [42] has been selected and the k-points setting has been applied with the coarse quality for all the energy minimizations in this work. For all the heterostructure surfaces, we have introduced 20 Å vacuum space in the z-axis to ensure full relaxation. Meanwhile, for all the geometry optimizations, we have set the following convergence criteria including the Hellmann-Feynman forces should be smaller than 0.001 eV/Å, the total energy difference and the inter-ionic displacement should not exceed 5×10^{-5} eV/atom, and 0.005 Å, respectively.

Data availability.

The data supporting the findings of this study are available within the article and its Supplementary Information. Source data are provided with this paper.

References

1. Yang W. et al. Electronic-structure tuning of water-splitting nanocatalysts. Trends Chem. **1**, 259–271 (2019).
2. Yang W. et al. Amorphous Ru nanoclusters onto Co-doped 1D carbon nanocages enables efficient hydrogen evolution catalysis. Chinese J. Catal. **43**, 110–115 (2022).
3. Zeng L. et al. Anti-dissolution Pt single site with Pt(OH)(O_3)/Co(P) coordination for efficient alkaline water splitting electrolyzer. Nat. Commun. **13**, 3822 (2022).

4. Zou X. & Zhang Y. Noble metal-free hydrogen evolution catalysts for water splitting. Chem. Soc. Rev. **44**, 5148–80 (2015).
5. Han N. et al. Nitrogen-doped tungsten carbide nanoarray as an efficient bifunctional electrocatalyst for water splitting in acid. Nat. Commun. **9**, 924 (2018).
6. Wang C. & Qi L. Heterostructured inter-doped ruthenium-cobalt oxide hollow nanosheet arrays for highly efficient overall water splitting. Angew. Chem. Int. Ed. **59**, 17219–17224 (2020).
7. Wang H. et al. Significantly enhanced overall water splitting performance by partial oxidation of Ir through Au modification in core-shell alloy structure. J. Am. Chem. Soc. **143**, 4639–4645 (2021).
8. Zhu J. et al. Regulative electronic states around ruthenium/ruthenium disulphide heterointerfaces for efficient water splitting in acidic media. Angew. Chem. Int. Ed. **60**, 12328–12334 (2021).
9. Li Y. et al. Recent advances on water-splitting electrocatalysis mediated by noble-metal-based nanostructured materials. Adv. Energy Mater. **10**, 1903120 (2020).
10. Chen D. et al. Ultralow Ru loading transition metal phosphides as high-efficient bifunctional electrocatalyst for a solar-to-hydrogen generation system. Adv. Energy Mater. **10**, 2000814 (2020).
11. Chen X. et al. Atomically dispersed ruthenium on nickel hydroxide ultrathin nanoribbons for highly efficient hydrogen evolution reaction in alkaline media. Adv. Mater. **33**, 2104764 (2021).
12. Zhang H. et al. Spontaneous ruthenium doping in hierarchical flower-like Ni_2P/NiO heterostructure nanosheets for superb alkaline hydrogen evolution. Chem. Eng. J. **417**, 128069 (2021).
13. Liu Z. et al. Charge redistribution of Ru nanoclusters on Co_3O_4 porous nanowire via the oxygen regulation for enhanced hydrogen evolution reaction. Nano Energy **85**, 105940 (2021).
14. Chen Q. Q. et al. Inlay of ultrafine Ru nanoparticles into a self-supported $Ni(OH)_2$ nanoarray for hydrogen evolution with low overpotential and enhanced kinetics. J. Mater. Chem. A **7**, 11062–11068 (2019).
15. Liu Y. et al. Ru modulation effects in the synthesis of unique rod-like Ni@Ni_2P-Ru heterostructures and their remarkable electrocatalytic hydrogen evolution performance. J. Am. Chem. Soc. **140**, 2731–2734 (2018).
16. Sun Y. et al. Modulating electronic structure of metal-organic frameworks by introducing atomically dispersed Ru for efficient hydrogen evolution. Nat. Commun. **12**, 1369 (2021).
17. Su J. et al. Ruthenium-cobalt nanoalloys encapsulated in nitrogen-doped graphene as active electrocatalysts for producing hydrogen in alkaline media. Nat. Commun. **8**, 14969 (2017).
18. Wang C. et al. Heterogeneous bimetallic sulfides based seawater electrolysis towards stable industrial-level large current density. Appl. Catal. B-Environ. **291**, 120071 (2021).
19. Liang C. et al. Exceptional performance of hierarchical Ni-Fe oxyhydroxide@NiFe alloy nanowire array electrocatalysts for large current density water splitting. Energy Environ. Sci. **13**, 86–95 (2020).
20. Cheng X. et al. Highly active, stable oxidized platinum clusters as electrocatalysts for the hydrogen evolution reaction. Energy Environ. Sci. **10**, 2450–2458 (2017).

21. Wu X. et al. Solvent-free microwave synthesis of ultra-small Ru-Mo_2C@CNT with strong metal-support interaction for industrial hydrogen evolution. Nat. Commun. **12**, 4018 (2021).
22. Li G. et al. The synergistic effect of Hf-O-Ru bonds and oxygen vacancies in Ru/HfO_2 for enhanced hydrogen evolution. Nat. Commun. **13**, 1270 (2022).
23. Zhuang L. et al. Tuning oxygen vacancies in two-dimensional iron-cobalt oxide nanosheets through hydrogenation for enhanced oxygen evolution activity. Nano Res. **11**, 3509–3518 (2018).
24. Li J. et al. Boosting electrocatalytic activity of Ru for acidic hydrogen evolution through hydrogen spillover strategy. ACS Energy Lett. **7**, 1330–1337 (2022).
25. Xu J. et al. Boosting the hydrogen evolution performance of ruthenium clusters through synergistic coupling with cobalt phosphide. Energy Environ. Sci. **11**, 1819–1827 (2018).
26. Xu K. et al. Regulating water-reduction kinetics in cobalt phosphide for enhancing HER catalytic activity in alkaline solution. Adv. Mater. **29**, 1606980 (2017).
27. Zhai P. et al. Engineering single-atomic ruthenium catalytic sites on defective nickel-iron layered double hydroxide for overall water splitting. Nat. Commun. **12**, 4587 (2021).
28. Li P. et al. Boosting oxygen evolution of single-atomic ruthenium through electronic coupling with cobalt-iron layered double hydroxides. Nat. Commun. **10**, 1711 (2019).
29. Wu Z. et al. Corrosion engineering on iron foam toward efficiently electrocatalytic overall water splitting powered by sustainable energy. Adv. Funct. Mater. **31**, 2010437 (2021).
30. Nie N. et al. Superfast synthesis of densely packed and ultrafine Pt-Lanthanide@KB via solvent-free microwave as efficient hydrogen evolution electrocatalysts. Small **17**, 2102879 (2021).
31. Rong C. et al. Electronic structure engineering of single-atom Ru sites via Co-N_4 sites for bifunctional pH-universal water splitting. Adv. Mater. **34**, 2110103 (2022).
32. Xiao X. et al. In situ growth of Ru nanoparticles on (Fe,Ni)$(OH)_2$ to boost hydrogen evolution activity at high current density in alkaline media. Small Methods **4**, 1900796 (2020).
33. Wu D. et al. Ultralow Ru incorporated amorphous cobalt-based oxides for high-current-density overall water splitting in alkaline and seawater media. Small **17**, 2102777 (2021).
34. Yuan S. et al. A universal synthesis strategy for single atom dispersed cobalt/metal clusters heterostructure boosting hydrogen evolution catalysis at all pH values. Nano Energy **59**, 472–480 (2019).
35. Yu X. et al. Highly disordered cobalt oxide nanostructure induced by sulfur incorporation for efficient overall water splitting. Nano Energy **71**, 104652 (2020).
36. Zhuang L. et al. Ultrathin iron-cobalt oxide nanosheets with abundant oxygen vacancies for the oxygen evolution reaction. Adv. Mater. **29**, 1606793 (2017).
37. Yu Z. Y. et al. Ni-Mo-O nanorod-derived composite catalysts for efficient alkaline water-to-hydrogen conversion via urea electrolysis. Energy Environ. Sci. **11**, 1890–1897 (2018).
38. Clark, S. J. et al. First principles methods using CASTEP. Z. Krist-cryst Mater. **220**, 567–570 (2005).

39. Perdew, J. P. et al. Generalized gradient approximation made simple. Phys. Rev. Lett. **77**, 3865–3868 (1996).
40. Hasnip, P. J. & Pickard, C. J. Electronic energy minimisation with ultrasoft pseudopotentials. Comput. Phys. Commun. **174**, 24–29 (2006).
41. Perdew, J. P. et al. Atoms, molecules, solids, and surfaces: Applications of the generalized gradient approximation for exchange and correlation. Phys. Rev. B **46**, 6671–6687 (1992).
42. Head, J. D. & Zerner, M. C. A Broyden-Fletcher-Goldfarb-Shanno optimization procedure for molecular geometries. Chem. Phys. Lett. **122**, 264–270 (1985).

Declarations

Acknowledgements

This work was financially supported by the National Key Research and Development Program of China (2020YFB1506300); National Natural Science Foundation of China (Grant Nos. 21625102, 21971017, 21922502, 22075018, 51991344, 52025025, 52072400); Beijing Institute of Technology Research Fund Program; The Natural Science Foundation of Hainan Province (2019RC166); Beijing Natural Science Foundation (Z190010).

Author contributions

X.F., B.W. and W.Y. directed the research and revised the manuscript. R.L. and X.L. designed and completed the experiments and data analysis. M.S. and B.H. were in charge of DFT calculations. Z.L. completed the part of electrochemical tests. X.Y. and L.L. conducted XRD characterization. J.W. and Y.L. performed the SEM characterization. R.L. completed the manuscript and all authors discussed the results and provided comments on the manuscript.

Competing interests

The authors declare no competing interests.

Additional information

Supplementary Information The online version contains supplementary material available at http://doi.org/10.xxxx/xxxxxxxx

Correspondence and requests for materials should be addressed to Wenxiu Yang, Bolong Huang or Bo Wang.

Peer review information *Nature Communications* thanks xxx and the other, anonymous, reviewer(s) for their contribution to the peer review of this work.

Publisher's note: Springer Nature remains neutral with regard to jurisdictional claims in published maps and institutional affiliations.

Figures

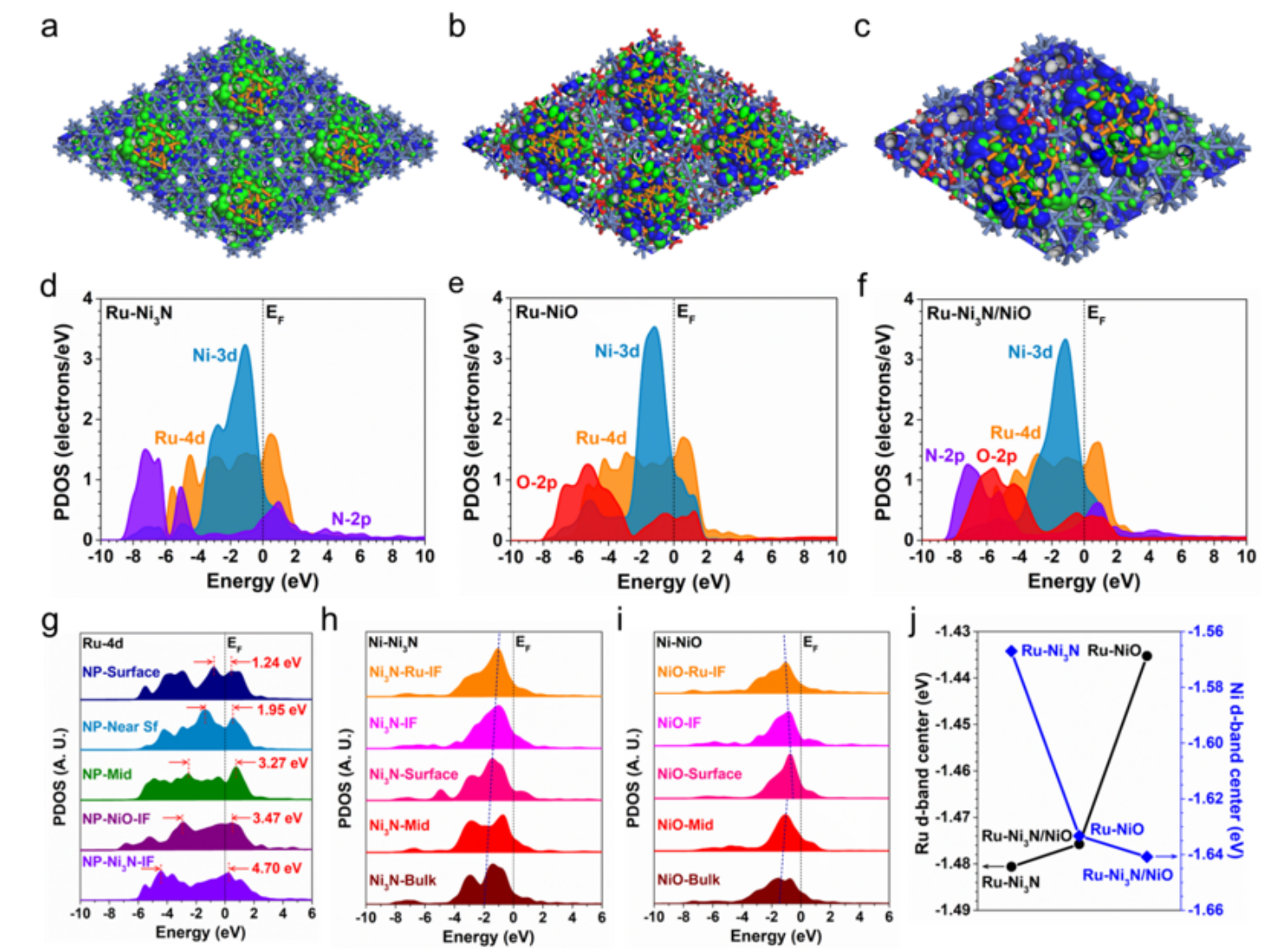

Figure 1

DFT calculations of electronic structure. The 3D contour plots of bonding and anti-bonding orbitals near the Fermi level for **a** Ru-Ni_3N, **b** Ru-NiO, and **c** Ru-Ni_3N/NiO. Light balls = Ni, Orange balls= Ru, Dark blue balls = N, Red balls = O. Blue isosurface = bonding orbitals and Green isosurface = anti-bonding orbitals. PDOSs of **d** Ru-Ni_3N, **e** Ru-NiO and **f** Ru-Ni_3N/NiO. **g** The site-dependent PDOS of Ru-4d in Ru-Ni_3N/NiO. **h** The site-dependent PDOS of Ni-3d in the Ni_3N part of Ru-Ni_3N/NiO. **i** The site-dependent PDOS of Ni-3d in the NiO part of Ru-Ni_3N/NiO. **j** The d-band center evolution.

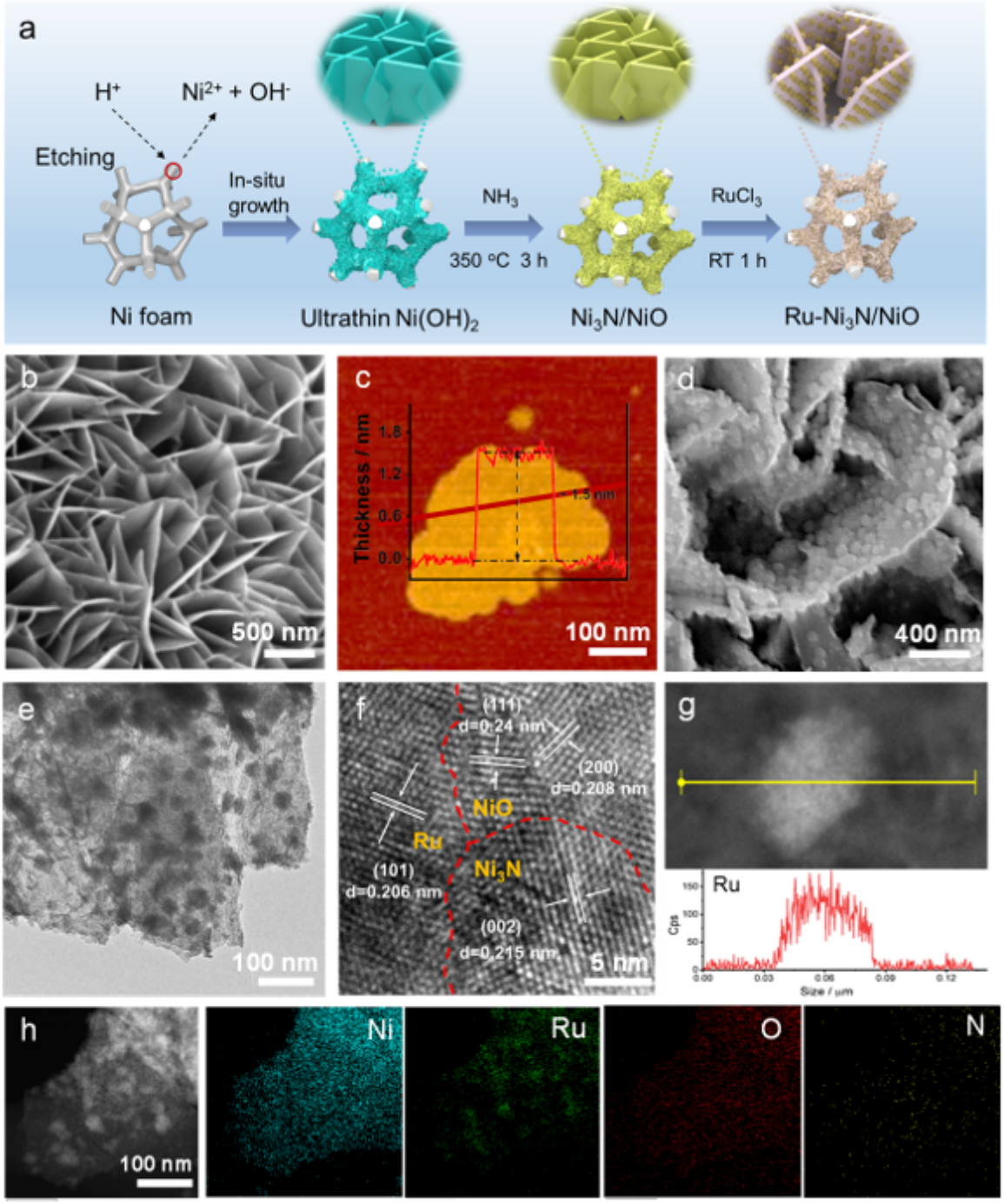

Figure 2

Formation process, morphology, and element characterizations of the obtained catalysts. a Schematic illustration of the formation of Ru-Ni_3N/NiO. **b** SEM and **c** AFM images of $Ni(OH)_2$. **d** SEM, **e** TEM and **f** HRTEM images of Ru-Ni_3N/NiO. **g** HAADF-STEM EDS line scan image of Ru nanoparticle for Ru-Ni_3N/NiO. **h** HAADF-STEM image for Ru-Ni_3N/NiO with elemental mapping images for Ni, Ru, O, and N elements.

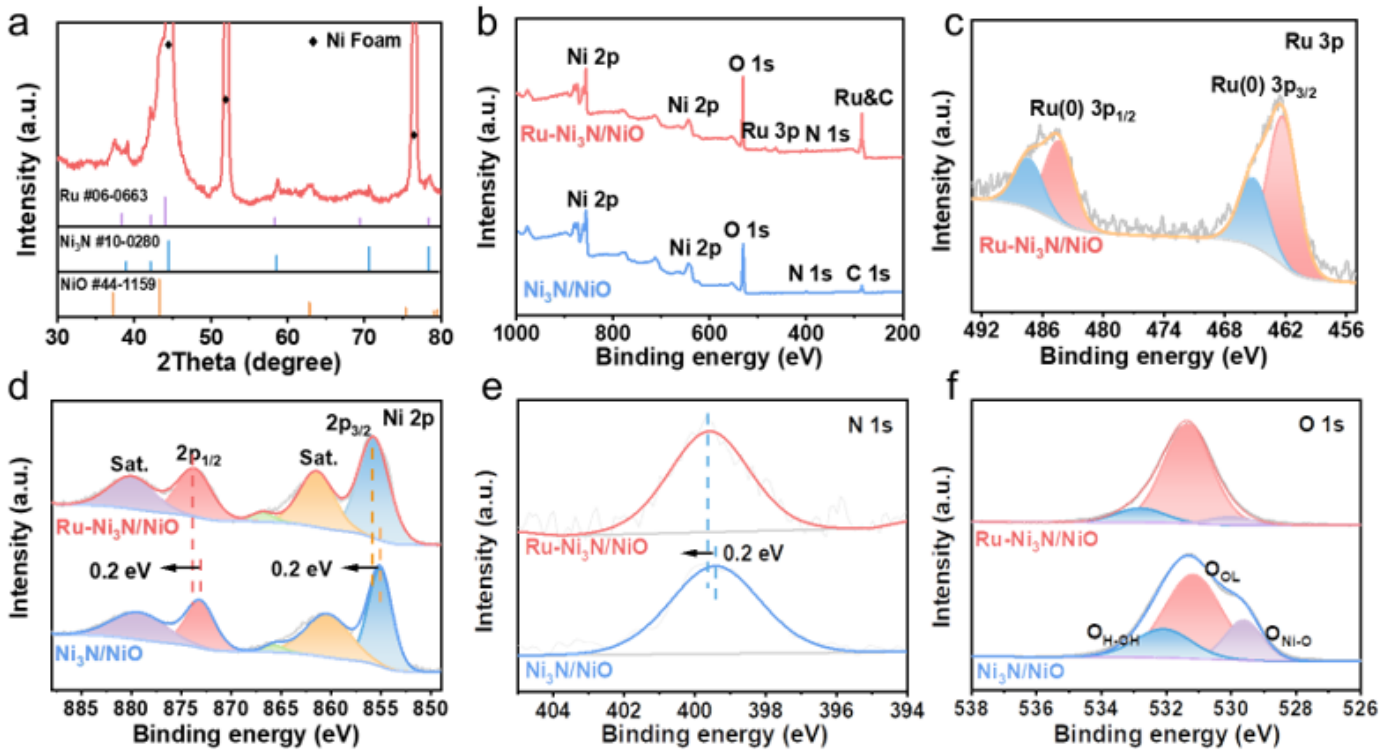

Figure 3

Structural characterizations of the obtained catalysts. a XRD pattern of Ru-Ni_3N/NiO. **b** survey spectra of Ru-Ni_3N/NiO and Ni_3N/NiO. **c** High-resolution Ru 3p spectrum of Ru-Ni_3N/NiO. High-resolution XPS spectra of Ru-Ni_3N/NiO and Ni_3N/NiO: **d** Ni 2p, **e** N 1s, and **f** O 1s.

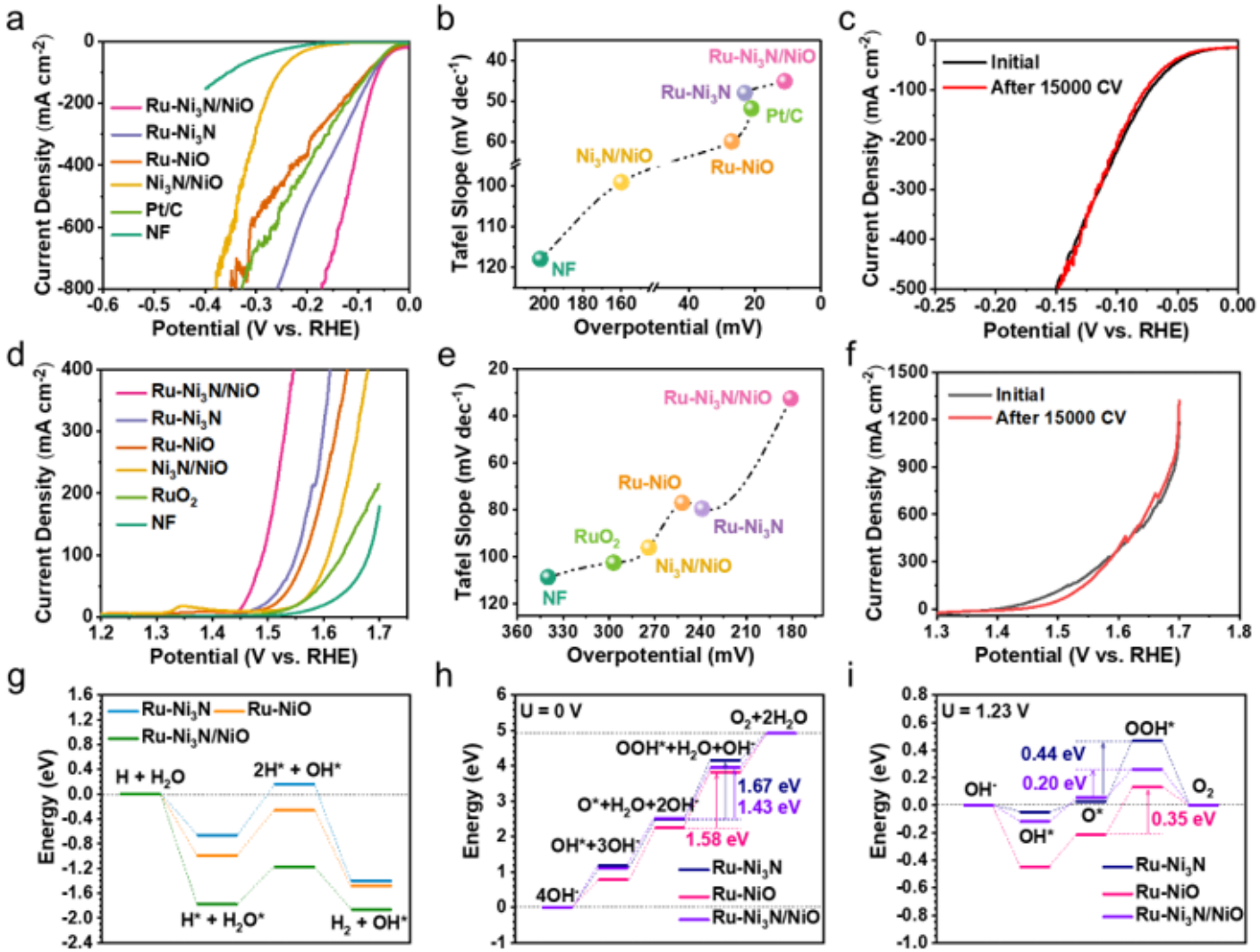

Figure 4

Electrocatalytic performances. **a** Polarization curves of different catalysts for HER. **b** The corresponding overpotential (@ 10 mA cm^{-2}) and Tafel slope of obtained catalysts for HER. **c** Polarization curves of Ru-Ni_3N/NiO for the HER before and after 15000 CV cycles. **d** Polarization curves of different catalysts for OER. **e** The corresponding overpotential (@ 10 mA cm^{-2}) and Tafel slope of obtained catalysts for OER. **f** Polarization curves of Ru-Ni_3N/NiO for the OER before and after 15000 CV cycles. **g** The reaction energy change for HER in the alkaline environment. **h** The reaction energy change for OER in the alkaline environment under U = 0 V. **i** The reaction energy change for OER in the alkaline environment under U = 1.23 V.

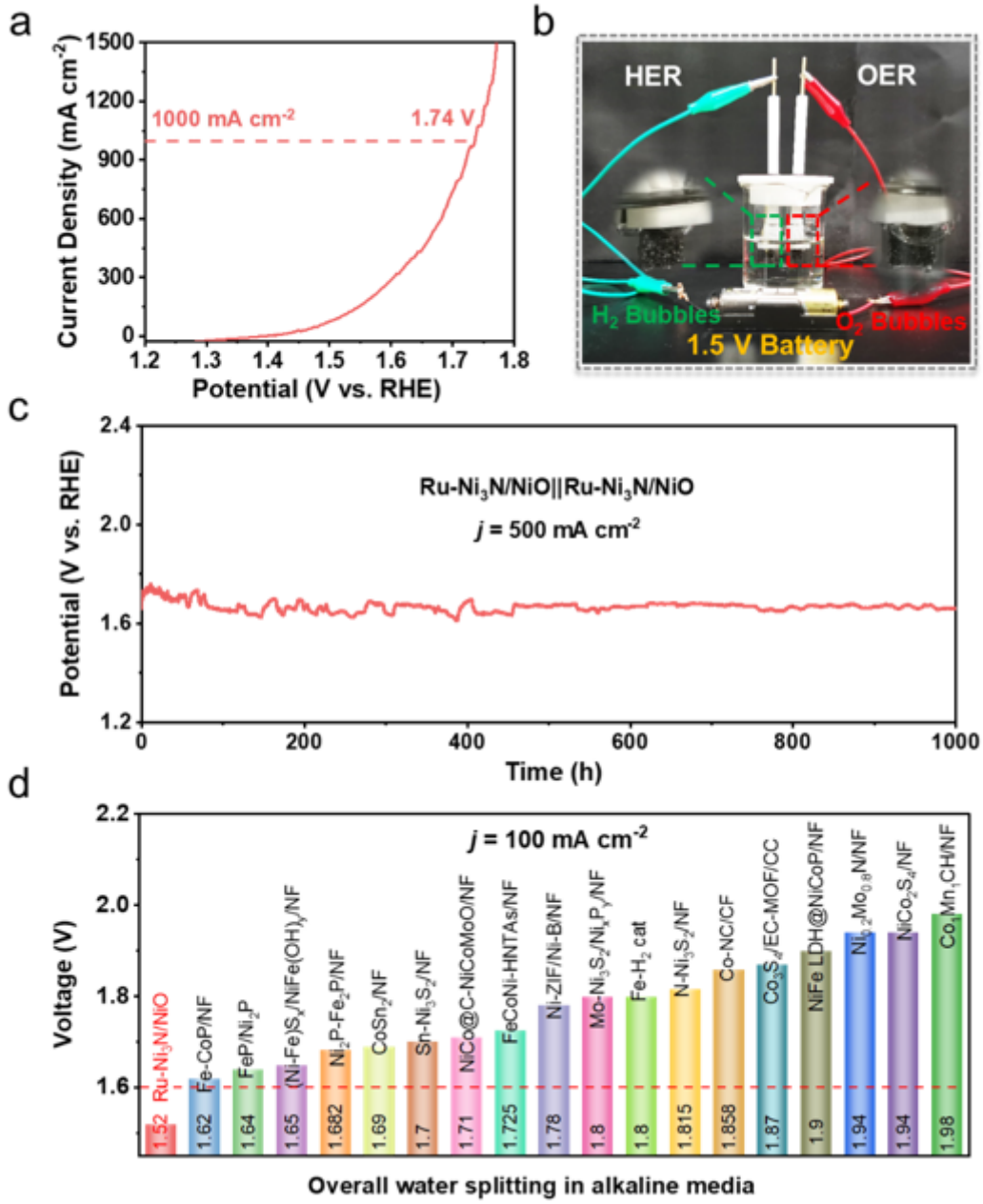

Figure 5

Performance in water electrolyzers device. a Overall water splitting activity of Ru-Ni_3N/NiO(+,-). **b** Photograph of overall water splitting using Ru-Ni_3N/NiO powered by a 1.5 V battery in 1.0 M KOH solution. **c** Chronopotentiometry curves of Ru-Ni_3N/NiO(+,-) at a constant current density of 500 mA cm^{-2}. **d** Comparison of the cell voltage at 100 mA cm^{-2} for Ru-Ni_3N/NiO(+,-) with previously reported catalyst.

Supplementary Files

This is a list of supplementary files associated with this preprint. Click to download.

- SI202208.docx
- floatimage6.png